The pulsatile flow of thermally developed non-Newtonian Casson fluid in a channel with constricted walls

Zainab Bukhari, Amjad Ali, Zaheer Abbas, et al.

View Online   Export Citation   CrossMark

ARTICLES YOU MAY BE INTERESTED IN

Numerical investigation of thermally developed MHD flow with pulsation in a channel with multiple constrictions
AIP Advances **11**, 055320 (2021); https://doi.org/10.1063/5.0052276

Magnetic field effect on Poiseuille flow and heat transfer of carbon nanotubes along a vertical channel filled with Casson fluid
AIP Advances **7**, 015036 (2017); https://doi.org/10.1063/1.4975219

Influences of Hall current and radiation on MHD micropolar non-Newtonian hybrid nanofluid flow between two surfaces
AIP Advances **10**, 055015 (2020); https://doi.org/10.1063/1.5145298
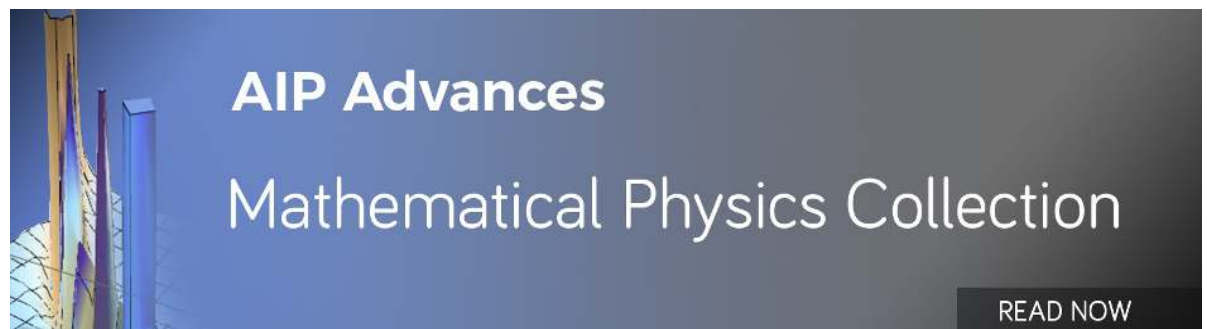
AIP Advances
Mathematical Physics Collection
READ NOW

The pulsatile flow of thermally developed non-Newtonian Casson fluid in a channel with constricted walls

Zainab Bukhari,[1,a]   Amjad Ali,[1]   Zaheer Abbas,[2]   and   Hamayun Farooq[1]

AFFILIATIONS

[1] Centre for Advanced Studies in Pure and Applied Mathematics, Bahauddin Zakariya University, Multan, Pakistan
[2] Department of Mathematics, The Islamia University of Bahawalpur, Bahawalpur 63100, Pakistan

[a] Author to whom correspondence should be addressed: zainabbukhari398@gmail.com

ABSTRACT

This article presents a numerical investigation of the pulsatile flow of non-Newtonian Casson fluid through a rectangular channel with symmetrical local constriction on the walls. The objective is to study the heat transfer characteristics of the said fluid flow under an applied magnetic field and thermal radiation. Such a study may find its application in devising treatments for stenosis in blood arteries, designing biomechanical devices, and controlling industrial processes with flow pulsation. Using the finite difference approach, the mathematical model is solved and is converted into the vorticity-stream function form. The impacts of the Hartman number, Strouhal number, Casson fluid parameter, porosity parameter, Prandtl number, and thermal radiation parameter on the flow profiles are argued. The effects on the axial velocity and temperature profiles are observed and argued. Some plots of the streamlines, vorticity, and temperature distribution are also shown. On increasing the values of the magnetic field parameter, the axial flow velocity increases, whereas the temperature decreases. The flow profiles for the Casson fluid parameter have a similar trend, and the profiles for the porosity parameter have an opposite trend to the flow profiles for the magnetic field parameter. The temperature decreases with an increase in the Prandtl number. The temperature increases with an increase in the thermal radiation parameter. The profile patterns are not perfectly uniform downstream of the constriction.

Nomenclatures

$\mathbf{B}$	uniform magnetic field
C_p	specific heat
D_a	porosity parameter
$\mathbf{E}$	electric field
J	current velocity
$\mathbf{J}$	electric field
k	thermal conductivity
M	Hartman number
Pr	Prandtl number
Rd	radiation parameter
Re	Reynolds number of the flow
St	Strouhal number
T	period of the flow pulsation

U	characteristic flow velocity
U	characteristic flow velocity
β	Casson fluid parameter
μ	dynamic viscosity
μ_m	magnetic permeability of the medium
v	kinematic viscosity
ρ	density
σ	electric conductivity

I. INTRODUCTION

In various engineering and biomechanical applications, non-Newtonian fluid (NNF) flows in constricted channels are of particular interest. Early studies related to the constricted channels discussed simple steady and laminar flows in the channel, such as Lee[1]

and Huwang.[2] Mahapatra et al.[3] studied unsteady laminar flows in a constricted channel. The next level of relevant studies involves the pulsating motion of the flow in a constricted channel, such as Tutty[4] and Mittal.[5] Isler et al.[6] discussed the pulsatile flow along with equilibrium states in a constricted channel. Bandyopadhay and Layek[7] numerically studied the pulsatile flow in a locally constricted channel in detail. The research of the pulsating motion of Newtonian and non-Newtonian flows also finds its applications in understanding the blood flow, especially in the stenotic arteries. Because of the pulse's cyclic nature, the blood flow in a living body is intrinsically unstable and pulsative. Its study is challenging in both experimental and computational research. The flow pattern may be laminar or turbulent due to the position and function of the blood vessels. If the Reynolds number is low, the blood flow is laminar and pulsatile in small arteries; however, the Reynolds number is usually high in large arteries, and the blood flow is turbulent. The wall shear stress (WSS) and pressure play a considerable role in hemodynamics in arteries. Therefore, it is crucial to comprehend the dynamics of these sorts of pulsatile flows. Clark[8] studied both pulsatile and non-pulsatile flows via nozzle style stenosis and stated highly disturbed flow statistics and the Reynolds number's effect on velocity fluctuations. Shirai and Masuda[9] numerically studied the passing of neutrophil through a rectangular channel with a moderate constriction. Chakravarty[10] discussed the unsteady pulsatile flow in an artery with an irregular surface. Liu and Yamaguchi[11] explained the waveform dependence of the pulsatile flow in the stenosed channel. Khair et al.[12] discussed the transition of a pulsatile flow from the laminar to the turbulent regime in the constricted channel. Hirtum[13] attempted to explain in detail the analytic modeling of the flow in constricted channels. Mustapha et al.[14] numerically simulated unsteady blood flow in an arterial section having a pair of stenosis.

In recent years, the analysis of non-Newtonian flows under the impact of the magnetic field has attained tremendous attention due to its large number of uses in medical science. Examples include the cosmetic industry, solidification of fluid crystals, extrusion of polymer liquids, cooling of a metallic plate in a bath, dying of textile and paper, petroleum industries, magnetohydrodynamic (MHD) pumps and generators, the motion of artificial dialysis, and biological liquids. To analyze several rheological possessions, some investigators have proposed diverse non-Newtonian liquid models, one of which is the Casson liquid model. Casson[15] proposed the Casson liquid model and established that it does not follow the Newtonian law of viscosity. The model was established to be more appropriate for rheological data than other NNF models, such as chocolate and blood flows. Sankar and Lee[16] discussed the impact of magnetohydrodynamics on pulsatile blood flow as Casson flow via slightly constricted arteries. Sankar et al.[17] examined the blood pulsatile flow in narrow arteries by treating blood flow as Casson fluid (CF) in the core layer and cell reduced plasma as Newtonian fluid (NF) in the exterior layer. Bali and Awasthi[18] examined the blood flow via a multi-stenosed artery under the impact of the applied magnetic field. Padma et al.[19] presented a model for the non-Newtonian blood flow, taking into account Jeffery fluid with a mild stenosis artery. Iqbal et al.[20] investigated the influence of an inclined magnetic field on micropolar CF over a stretching sheet with the effects of viscous dissipation. Reddy et al.[21] analyzed the molecular dynamics analysis on transient MHD Casson liquid flow dispersion past a vertical

radiative cylinder. Shit and Majee[22] studied the pulsatile MHD blood flow and heat transfer in arteries with the vibrating body. Some inquiries involving the peristaltic motion of NNF and NF are provided in Refs. 23–26.

The consideration of heat transfer of Newtonian and NNF in a channel has become essential due to its tremendous applications in engineering and biomechanics. Moschandreu and Zamir[27] studied the pulsatile flow within a pipe among constant heat flux at the wall to define how pulsation affects the heat transfer rate and how the phenomenon be influenced by the Prandtl number and the frequency of pulsation. Ji et al.[28] performed experiments to enhance the heat transfer in pulsating flow in a heated rectangular cylinder. Elshafei et al.[29] stated that the heat transfer method would be deteriorated by pulsations related to the results found under steady flow. Blythman et al.[30] explored the heat transfer of pulsating flow in a rectangular channel. Aman et al.[31] evaluated the heat transfer in an unsteady MHD flow of CF over a vertical oscillated plate. Hussanan et al.[32] analyzed CF under the impact of thermal radiation on the wall via an oscillating vertical plate among Newtonian heating. Srinivas et al.[33] explored the influence of thermal radiation, diffusion, and chemical reaction of a CF's hydro-magnetic pulsatile flow in a porous channel. Ullah et al.[34] analyzed the influence of chemical reaction, viscous dissipation, and heat generation of CF over a cylinder subject to suction/blowing. Khan et al.[35] argued the heat transfer characteristics of SWCNT and MWCNT for CF's mixed convection Poiseuille flow with a vertical channel. Ahmed and Arafa[36] presented a mathematical formulation and numerical simulations of an unsteady MHD non-Newtonian nanofluid flow and entropy generation over a vertical plate using the fractional derivatives approach. Kumar et al.[37] analyzed the comparative (3D) model for Casson-nanofluid and Carreau-nanofluid flows due to a flat body in a MHD stratified environment. For steady and pulsatile flows, Ali et al.[38] investigated the flow behavior and CF's electrically conducted separation region via a 2D porous channel that followed Darcy's law.

The objective of the present work is to numerically explore the heat transfer in the pulsatile flow of non-Newtonian CF in a locally constricted channel in the presence of an applied magnetic field, which is not considered yet. The unsteady governing model is converted by using the vorticity-stream function approach and solved using a computational scheme based on the finite difference method (FDM). The impact of the Hartman number (M), Strouhal number (St), Casson parameter (β), porosity parameter (D_a), Prandtl number (Pr), and radiation parameter (Rd) on the flow profiles is discussed. In particular, the influence of the relevant flow controlling parameters on the axial velocity and temperature profiles is observed and argued.

The subsequent part of the article is organized as follows: Sec. II explains the mathematical formulation, boundary conditions, and transformation of the model in terms of vorticity-stream function. In Sec. III, the numerical method is defined. The outcomes and relevant discussion are presented in Sec. IV. Finally, in Sec. V, the findings are summarized.

II. MATHEMATICAL FORMULATION

We study an incompressible electrically conducting fluid, which is supposed to be laminar at the Reynolds number of 700,
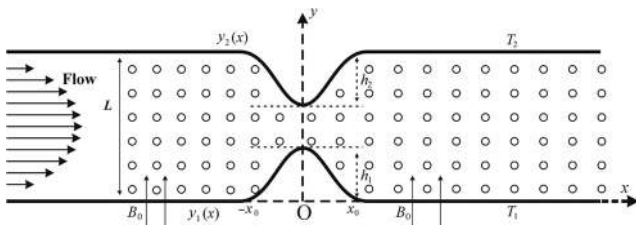
FIG. 1. Pulsatile Casson fluid flow channel with constricted walls having porous medium.

flowing through a rectangular porous channel. As shown in Fig. 1, the lower and upper walls of the channel have constrictions. **B** (uniform magnetic field) is applied to the walls perpendicularly, whereas, **J** (electric field) is applied normally to the flow plane. Therefore, we consider flow direction to be along the $\tilde{x}$-axis and the direction of **B** is along the $\tilde{y}$-axis by taking Cartesian coordinate system $(\tilde{x}, \tilde{y})$. The temperature due to the thermal radiation at the lower and upper walls are T_1 and T_2, respectively. The rheological equation for incompressible CF is as follows:[39]

$$\tau_{ij} = \begin{cases} 2\left(\mu_\beta + P_y/\sqrt{2\pi}\right)e_{ij} & \pi > \pi_c \\ 2\left(\mu_\beta + P_y/\sqrt{2\pi_c}\right)e_{ij} & \pi < \pi_c \end{cases},$$

where $\pi = e_{ij}e_{ij}$ and e_{ij} are the (i,j) th component of deformation rate, μ_β denotes the NNF's plastic dynamic viscosity, P_y denotes the fluid's yield stress, π expresses the product of the component of deformation rate itself, and π_c denotes a critical value dependent on the NNF model of this product.

The unsteady incompressible Navier–Stokes equations representing the flow phenomenon are given as follows:

The continuity equation,

$$\frac{\partial \tilde{u}}{\partial \tilde{x}} + \frac{\partial \tilde{v}}{\partial \tilde{y}} = 0, \tag{1}$$

the momentum equations,

$$\frac{\partial \tilde{u}}{\partial \tilde{t}} + \tilde{u}\frac{\partial \tilde{u}}{\partial \tilde{x}} + \tilde{v}\frac{\partial \tilde{u}}{\partial \tilde{y}} = -\frac{1}{\rho}\frac{\partial \tilde{p}}{\partial \tilde{x}} + v\left(1 + \frac{1}{\beta}\right)\nabla^2 \tilde{u} + \frac{1}{\rho}(\mathbf{J} \times \mathbf{B})_x - \frac{v}{k}\tilde{u}, \tag{2}$$

$$\frac{\partial \tilde{v}}{\partial \tilde{t}} + \tilde{u}\frac{\partial \tilde{v}}{\partial \tilde{x}} + \tilde{v}\frac{\partial \tilde{v}}{\partial \tilde{y}} = -\frac{1}{\rho}\frac{\partial \tilde{p}}{\partial \tilde{y}} + v\left(1 + \frac{1}{\beta}\right)\nabla^2 \tilde{v} - \frac{v}{k}\tilde{v}, \tag{3}$$

and the heat equation,

$$\frac{\partial \tilde{T}}{\partial \tilde{t}} + \tilde{u}\frac{\partial \tilde{T}}{\partial \tilde{x}} + \tilde{v}\frac{\partial \tilde{T}}{\partial \tilde{y}} = \frac{k}{\rho C_p}\nabla^2 \tilde{T} - \frac{1}{\rho C_p}\frac{\partial q}{\partial \tilde{y}}, \tag{4}$$

where $q = -\left(\frac{4\sigma}{3k}\frac{\partial \tilde{T}^4}{\partial \tilde{y}}\right)$ is the radiative heat flux. Expanding $\tilde{T}^4$ about T_∞ and ignoring higher-order terms, we get

$$\tilde{T}^4 \cong 4T_\infty^3 \tilde{T} - 3T_\infty^4.$$

Then $q = -\left(\frac{4\sigma}{3k}4T_\infty^3\frac{\partial \tilde{T}}{\partial \tilde{y}}\right)$ and $\frac{\partial q}{\partial \tilde{y}} = -\left(\frac{16\sigma}{3k}T_\infty^3\frac{\partial^2 \tilde{T}}{\partial \tilde{y}^2}\right)$.

Equation (4) becomes

$$\frac{\partial \tilde{T}}{\partial \tilde{t}} + \tilde{u}\frac{\partial \tilde{T}}{\partial \tilde{x}} + \tilde{v}\frac{\partial \tilde{T}}{\partial \tilde{y}} = \frac{k}{\rho C_p}\left(\frac{\partial^2 \tilde{T}}{\partial \tilde{x}^2} + \frac{\partial^2 \tilde{T}}{\partial \tilde{y}^2}\right) + \frac{16\sigma T_\infty^3}{3k\rho C_p}\frac{\partial^2 \tilde{T}}{\partial \tilde{y}^2}, \tag{5}$$

where $\tilde{u}$ and $\tilde{v}$ are the velocity components along $\tilde{x}$- and $\tilde{y}$-axes, respectively, $\tilde{p}$ denotes the pressure, ρ denotes the density, U denotes the characteristic flow velocity, v denotes the kinematic viscosity, β denotes the CF parameter, and $\tilde{T}$ denotes the temperature. k denotes the thermal conductivity, C_p denotes the specific heat, $\mathbf{J} \equiv (J_x, J_y, J_z)$ denotes current velocity, $\mathbf{B} \equiv (0, B_0, 0)$ denotes the magnetic field, B_0 denotes the strength of the uniform magnetic field, σ denotes electric conductivity, μ denotes dynamic viscosity, and μ_m denotes the magnetic permeability of the medium. If $\mathbf{E} \equiv (E_x, E_y, E_z)$ denotes the electric field such that the electric current flows along the normal to the plane of the flow, then, $\mathbf{E} \equiv (0, 0, E_z)$. Moreover, from Ohm's law,

$$J_x = 0, J_y = 0, J_z = \sigma(E_z + \tilde{u}B_0). \tag{6}$$

For the steady flow, Maxwell's equation $\nabla \times \mathbf{E} = 0$ implies that E_z is constant. For the current study, we suppose that $E_z = 0$. Then, Eq. (6) gives $J_z = \sigma \tilde{u}B_0$. Therefore, $\mathbf{J} \times \mathbf{B} = -\sigma \tilde{u}B_0^2$. Hence, Eqs. (2) and (3) become

$$\frac{\partial \tilde{u}}{\partial \tilde{t}} + \tilde{u}\frac{\partial \tilde{u}}{\partial \tilde{x}} + \tilde{v}\frac{\partial \tilde{u}}{\partial \tilde{y}} = -\frac{1}{\rho}\frac{\partial \tilde{p}}{\partial \tilde{x}} + v\left(1 + \frac{1}{\beta}\right)\nabla^2 \tilde{u} - \frac{1}{\rho}\sigma \tilde{u}B_0^2 - \frac{v}{k}\tilde{u}. \tag{7}$$

The following quantities are considered to obtain the dimensionless form of the governing model:

$$x = \frac{\tilde{x}}{L}, y = \frac{\tilde{y}}{L}, u = \frac{\tilde{u}}{U}, v = \frac{\tilde{v}}{U}, t = \frac{\tilde{t}}{T}, D_a = \frac{v}{U\sqrt{k}}, \theta = \frac{\tilde{T} - T_2}{T_1 - T_2}$$

$$p = \frac{\tilde{p}}{\rho U^2}, \text{Re} = \frac{UL}{v}, St = \frac{L}{UT}, M = B_0 L\sqrt{\frac{\sigma}{\rho v}}, \tag{8}$$

$$Pr = \frac{\mu C_p}{k}, Rd = \frac{16\sigma T_\infty^3}{3k\rho C_p}.$$

Here, T is the period of the flow pulsation, Re is the Reynolds number of the flow, St is the Strouhal number, M is the Hartman number, D_a is the porosity parameter, U is the characteristic flow velocity, Pr is the Prandtl number, and Rd is the radiation parameter.

Equations (1)–(3) and (5) are converted to following equations, respectively, by using quantities given in (8):

$$\frac{\partial u}{\partial x} + \frac{\partial u}{\partial y} = 0, \tag{9}$$

$$St\frac{\partial u}{\partial t} + u\frac{\partial u}{\partial x} + v\frac{\partial u}{\partial y} = -\frac{\partial p}{\partial x} + \frac{1}{\text{Re}}\left(1 + \frac{1}{\beta}\right)\nabla^2 u - \frac{M^2}{\text{Re}}u - \text{Re}D_a^2 u, \tag{10}$$

$$St\frac{\partial v}{\partial t} + u\frac{\partial v}{\partial x} + v\frac{\partial v}{\partial y} = -\frac{\partial p}{\partial y} + \frac{1}{\text{Re}}\left(1 + \frac{1}{\beta}\right)\nabla^2 v - \text{Re}D_a^2 v, \tag{11}$$

$$St\frac{\partial \theta}{\partial t} + u\frac{\partial \theta}{\partial x} + v\frac{\partial \theta}{\partial y} = \frac{1}{\text{Re}}\frac{1}{Pr}\left(\frac{\partial^2 \theta}{\partial x^2} + \frac{\partial^2 \theta}{\partial y^2} + Rd\frac{\partial^2 \theta}{\partial y^2}\right). \tag{12}$$

A. Channel wall geometry

The channel walls are defined by

$$y_1(x) = \begin{cases} \frac{h_1}{2}\left[1 + \cos\left(\frac{\pi x}{x_0}\right)\right], & |x| \le x_0, \\ 0, & |x| > x_0 \end{cases}$$

$$y_2(x) = \begin{cases} 1 - \frac{h_2}{2}\left[1 + \cos\left(\frac{\pi x}{x_0}\right)\right], & |x| \le x_0, \\ 1, & |x| > x_0 \end{cases}$$ (13)

where the lower and upper walls are represented by $y = y_1(x)$ and $y = y_2(x)$ with constriction's height h_1 and h_2, respectively. The constrictions are spanned from $x = -x_0$ to $x = x_0$ with its center at $x = 0$. Thus, the length of a constriction is $2x_0$.

B. Vorticity-stream function formulation

Dimensionless form of the momentum equation is transformed from primitive variables (u, v) to vorticity-stream functions (ψ, ω) as

$$u = \frac{\partial \psi}{\partial y}, v = -\frac{\partial \psi}{\partial x}, \omega = \frac{\partial v}{\partial x} - \frac{\partial u}{\partial y}.$$ (14)

To compute the WSS, the expression is given as

$$\tau = \mu \hat{n} \times \omega_{wall},$$ (15)

where $\hat{n}$ is the normal vector and ω_{wall} is the vorticity at the wall.[40] As vorticity and WSS are orthogonal to each other, the expression of vorticity can also be used to measure the WSS.[41]

By taking the derivative of Eq. (10) w.r.t. "y" and Eq. (11) w.r.t. "x", then subtracting, we get

$$St\frac{\partial}{\partial t}\left(\frac{\partial v}{\partial x} - \frac{\partial u}{\partial y}\right) + u\frac{\partial}{\partial x}\left(\frac{\partial v}{\partial x} - \frac{\partial u}{\partial y}\right) + v\frac{\partial}{\partial y}\left(\frac{\partial v}{\partial x} - \frac{\partial u}{\partial y}\right)$$
$$= \frac{1}{Re}\left[\frac{\partial^2}{\partial x^2}\left(\frac{\partial v}{\partial x} - \frac{\partial u}{\partial y}\right) + \frac{\partial^2}{\partial y^2}\left(\frac{\partial v}{\partial x} - \frac{\partial u}{\partial y}\right)\right]\left(1 + \frac{1}{\beta}\right)$$
$$- \frac{M^2}{Re}\frac{\partial u}{\partial y} + ReD_a^2\omega.$$ (16)

Using the quantities (14), the following vorticity transport equation is obtained:

$$St\frac{\partial\omega}{\partial t} + \frac{\partial\psi}{\partial y}\frac{\partial\omega}{\partial x} - \frac{\partial\psi}{\partial x}\frac{\partial\omega}{\partial y} = \frac{1}{Re}\left[\frac{\partial^2\omega}{\partial x^2} + \frac{\partial^2\omega}{\partial y^2}\right]\left(1 + \frac{1}{\beta}\right)$$
$$+ \frac{M^2}{Re}\frac{\partial^2\psi}{\partial y^2} + ReD_a^2\omega.$$ (17)

In addition, for the stream function (ψ), the Poisson equation is given as

$$\frac{\partial^2\psi}{\partial x^2} + \frac{\partial^2\psi}{\partial y^2} = -\omega,$$ (18)

whereas ω and ψ are the non-primitive variables.

C. Transformation of the coordinates

The constricted portion of the channel is transformed into a straight one by incorporating the following coordination transformation:

$$\xi = x, \eta = \frac{y - y_1(x)}{y_2(x) - y_1(x)}.$$ (19)

By using (19), the lower and upper walls of the channel are defined by $\eta = 0$ and $\eta = 1$, respectively, and Equations (17), (18), and (12) are converted into the new coordinate system (ξ, η) given in the following equations:

$$St\frac{\partial\omega}{\partial t} + u\left(\frac{\partial\omega}{\partial\xi} - Q\frac{\partial\omega}{\partial\eta}\right) + vD\frac{\partial\omega}{\partial\eta}$$
$$= \frac{1}{Re}\left(1 + \frac{1}{\beta}\right)\left[\frac{\partial^2\omega}{\partial\xi^2} - (P - 2QR)\frac{\partial\omega}{\partial\eta} - 2Q\frac{\partial^2\omega}{\partial\xi\partial\eta}\right.$$
$$\left. + (Q^2 + D^2)\frac{\partial^2\omega}{\partial\eta^2}\right] + \frac{M^2}{Re}D^2\frac{\partial^2\psi}{\partial\eta^2} + ReD_a^2\omega(20),$$ (20)

$$\frac{\partial^2\psi}{\partial\xi^2} - (P - 2QR)\frac{\partial\psi}{\partial\eta} - 2Q\frac{\partial^2\psi}{\partial\xi\partial\eta} + (Q^2 + D^2)\frac{\partial^2\psi}{\partial\eta^2} = -\omega,$$ (21)

$$St\frac{\partial\theta}{\partial t} + u\left(\frac{\partial\theta}{\partial\xi} - Q\frac{\partial\theta}{\partial\eta}\right) + vD\frac{\partial\theta}{\partial\eta}$$
$$= \frac{1}{RePr}\left[\frac{\partial^2\theta}{\partial\xi^2} - (P - 2QR)\frac{\partial\theta}{\partial\eta} - 2Q\frac{\partial^2\theta}{\partial\xi\partial\eta}\right.$$
$$\left. + (Q^2 + D^2 + RdD^2)\frac{\partial^2\theta}{\partial\eta^2}\right],$$ (22)

where

$$P = P(\xi, \eta) = \frac{\eta y_2''(\xi) + (1 - \eta)y_1''(\xi)}{y_2(\xi) - y_1(\xi)},$$
$$Q = Q(\xi, \eta) = \frac{\eta y_2'(\xi) + (1 - \eta)y_1'(\xi)}{y_2(\xi) - y_1(\xi)},$$ (23)
$$R = R(\xi) = \frac{y_2'(\xi) - y_1'(\xi)}{y_2(\xi) - y_1(\xi)}, D = D(\xi) = \frac{1}{y_2(\xi) - y_1(\xi)}.$$

The velocity components u and v take the form

$$u = D(\xi)\frac{\partial\psi}{\partial\eta}, v = Q(\xi, \eta)\frac{\partial\psi}{\partial\eta} - \frac{\partial\psi}{\partial\xi}.$$ (24)

D. Boundary conditions

For obtaining the boundary conditions for the flow problem under consideration, the dimensionless form of Eq. (7) is solved. For the steady case, the flow between two parallel plates in the presence of B_0 and E_z, the equation of motion (2) becomes

$$\rho\nu\left(1 + \frac{1}{\beta}\right)\frac{\partial^2\tilde{u}}{\partial\tilde{y}^2} - \sigma\tilde{u}B_0^2 - \rho\frac{\nu}{k}\tilde{u} = \frac{\partial\tilde{p}}{\partial\tilde{x}} + \sigma E_z B_0.$$ (25)

Here, E_z and $\frac{\partial\tilde{p}}{\partial\tilde{x}}$ are constants and all the other variables depend only on $\tilde{y}$.

Now, we non-dimensionalize Eq. (25) by using the dimensionless quantities (8), and we get

$$g\frac{d^2u}{dy^2} - M_1^2 u = \frac{L^2}{\rho v U}\left(\frac{\partial \tilde{p}}{\partial \tilde{x}} + \sigma E_z B_0\right), \qquad (26)$$

where $g = \left(1 + \frac{1}{\beta}\right)$ and $M_1^2 = \left(M^2 + Re^2 Da^2\right)$. Equation (26) has the following solution:

$$u(y) = \frac{1}{8}\frac{M^2}{M_1^2}\left[\frac{\cosh\left(\frac{M}{2}\right)\left[\cosh\left(\frac{M_1}{2\sqrt{g}}\right) - \cosh\left(\frac{M_1}{\sqrt{g}}\left(y - \frac{1}{2}\right)\right)\right]}{\sinh^2\left(\frac{M}{4}\right)\cosh\left(\frac{M_1}{2\sqrt{g}}\right)}\right],$$
$$v = 0, M \neq 0 \qquad (27)$$

where

$$\frac{M^2\cosh\left(\frac{M}{2}\right)}{8\sinh^2\left(\frac{M}{4}\right)} = -\frac{L^2}{\rho v U}\left(\frac{\partial \tilde{p}}{\partial \tilde{x}} + \sigma E_z B_0\right). \qquad (28)$$

The outlet boundary conditions are treated as for fully developed flows. For the pulsatile flow, the flow is considered sinusoidal,

$$u(y,t) = u(y)[1 + \sin(2\pi t)], v = 0. \qquad (29)$$

Furthermore, $u = 0$ and $v = 0$ (i.e., no-slip conditions) are considered on the walls.

The initial condition for the stream function (ψ) and the vorticity (ω) at the walls in the (ξ, η) system are given by

$$\psi = 0, \quad \text{for all } t \leq 0$$
$$\omega = 0, \quad \text{for all } t \leq 0$$

The resulting solution with necessary manipulations and transformation as defined in (19) produces the following boundary conditions. The boundary conditions for ψ in the (ξ, η) system are given as follows:

For $M \neq 0$,

$$\psi = \left[\frac{M^2\sqrt{g}\cosh\left(\frac{M}{2}\right)\left(\frac{M_1}{\sqrt{g}}\cosh\left(\frac{M_1}{2\sqrt{g}}\right)\eta - \sinh\left(\frac{M_1}{\sqrt{g}}\left(\eta - \frac{1}{2}\right)\right)\right)}{8M_1^3\sinh^2\left(\frac{M}{4}\right)\cosh\left(\frac{M_1}{2\sqrt{g}}\right)}\right]$$
$$\times [1 + \varepsilon\sin(2\pi t)], \qquad (30)$$

for $M = 0$ and $Da = 0$,

$$\psi = \frac{1}{6g}\left(3\eta^2 - 2\eta^3\right)[1 + \varepsilon\sin(2\pi t)], \qquad (31)$$

and for $M = 0$ and $Da \neq 0$,

$$\psi = \frac{2}{Re^2 Da^2}\left[\eta - \frac{\sqrt{g}}{ReDa}\left(\sinh(g_1) - \cosh(g_1)\tanh\left(\frac{g_1}{2}\right)\right)\right]$$
$$\times [1 + \varepsilon\sin(2\pi t)]. \qquad (32)$$

Here,

$$g = \left(1 + \frac{1}{\beta}\right), M_1^2 = \left(M^2 + Re^2 Da^2\right), g_1 = \frac{ReDa\eta}{\sqrt{g}},$$

and ε is the amplitude of the sinusoidal flow pulsation. $\varepsilon = 0$ for the steady flow, and $\varepsilon = 1$ for the pulsatile flow conditions. The wall boundary conditions for ψ are obtained at the upper and lower walls using $\eta = 0$ and $\eta = 1$, respectively, in (25)–(27).

The wall boundary conditions for ω in the (ξ, η) system, obtained from Eq. (14), are given by

$$\omega = -\left[\left(Q^2 + D^2\right)\frac{\partial^2\psi}{\partial\eta^2}\right]_{\eta=0,1}. \qquad (33)$$

The wall boundary conditions for θ in (ξ, η) system are given by

$$\left.\begin{array}{l}\theta = 1, \text{ at } \eta = 0 \\ \theta = 0, \text{ at } \eta = 1\end{array}\right\}. \qquad (34)$$

As for fully developed flows, the outlet boundary conditions are viewed. In addition, on the walls, no-slip conditions are considered.

III. NUMERICAL METHOD

The numerical solution of Eqs. (20)–(22) subject to the boundary conditions defined in Sec. II D is computed using FDM over a uniform structured grid. The computational domain is taken as $\{(\xi, \eta)|\xi \in [-x_1, x_1] \text{ and } \eta \in [0, 1]\}$. To ensure the stability of the numerical scheme, the step sizes are taken as follows: $\Delta t = 0.000\,25$ for the steady case, and $\Delta t = 0.000\,05$ for the pulsatile flow with $\Delta\xi = 0.05$, and $\Delta\eta = 0.02$. Thus, the domain is discretized by a grid of 400×50 elements. Furthermore, the length of each of the symmetric constriction is considered as $2x_0 = 4$ with heights $h1 = h2 = 0.35$; hence, the channel width, therefore, remains 30% at the throat of the constriction of the channel width. The solution at time level l is known, whereas the solution at each time level $l + 1$, for $l = 0, 1, 2, \ldots$, is computed. At each time level $l + 1$, first, Eq. (21) is solved for the stream function $\psi = \psi(\xi, \eta)$ using the central differences for the discretization of the space derivatives and the well-known TDMA (Tri-Diagonal Matrix Algorithm) for the linear system. Second, Eqs. (22) and (20) are solved for $\omega = \omega(\xi, \eta)$ and $\theta = \theta(\xi, \eta)$, respectively, using the well-known ADI (Alternating Direction Implicit) scheme. For this, the time derivative is discretized using the forward/backward difference. The initial conditions for ψ, ω, and θ at time level $l = 0$ are set as zero.

By discretizing, Eq. (21) at any time level $l + 1$, where $l = 0, 1, 2, \ldots$, and skipping the superscript $l + 1$ from ψ for simplicity and maintaining the uniformity, takes the form

$$\frac{\psi_{i+1,j} - 2\psi_{i,j} + \psi_{i-1,j}}{(d\xi)^2} - (P_{i,j} - 2Q_{i,j}R_i)\frac{\psi_{i,j+1} - \psi_{i,j-1}}{d\eta}$$
$$- 2Q_{i,j}\frac{\psi_{i+1,j+1} - \psi_{i-1,j+1} - \psi_{i+1,j-1} + \psi_{i-1,j-1}}{4d\xi d\eta}$$
$$+ \left(Q_{i,j}^2 + D_i^2\right)\frac{\psi_{i,j+1} - 2\psi_{i,j} + \psi_{i,j-1}}{(d\eta)^2} = -\omega_{i,j}^l. \qquad (35)$$

After rearranging, Eq. (35) takes the form

$$a(j)\psi_{i,j-1} + b(j)\psi_{i,j} + c(j)\psi_{i,j+1} = s(j) \qquad (36)$$

where $a(j)$, $b(j)$, $c(j)$, and $s(j)$ are given as follows:

$$a(j) = \frac{P_{i,j} - 2Q_{i,j}R_i}{2d\eta} + \frac{Q_{i,j}^2 + D_i^2}{(d\eta)^2},$$

$$b(j) = -\frac{2}{(d\xi)^2} - \frac{2}{(d\eta)^2}\left(Q_{i,j}^2 + D_i^2\right),$$

$$c(j) = -\frac{P_{i,j} - 2Q_{i,j}R_i}{2d\eta} + \frac{Q_{i,j}^2 + D_i^2}{(d\eta)^2}, \quad (37)$$

$$s(j) = -\omega_{i,j}^l - \left(\frac{\psi_{i+1,j} + \psi_{i-1,j}}{(d\xi)^2}\right)$$
$$+ 2Q_{i,j}\frac{\psi_{i+1,j+1} - \psi_{i-1,j+1} - \psi_{i+1,j-1} + \psi_{i-1,j-1}}{4d\eta d\xi}.$$

For every $i = 2, 3, \ldots, n-1$, Eq. (36) represents a linear tridiagonal system (for $j = 2, 3, \ldots, m-1$). TDMA with the over–relaxation parameter $\lambda = 1.3$ is used for solving the system.

The vorticity at the upper and lower walls are given by, for $i = 1, 2, 3, \ldots, n$,

$$\omega_{i,1}^l = -2\left(Q_{i,1}^2 + D_i^2\right)\frac{\psi_{i,2} - \psi_{i,1}}{(d\eta)^2},$$
$$\omega_{i,m}^l = -2\left(Q_{i,m}^2 + D_i^2\right)\frac{\psi_{i,m-1} - \psi_{i,m}}{(d\eta)^2}, \quad (38)$$

For solving Eq. (20), the solution is computed at the time level $l + 1/2$ using the solution at the time level l, for $l = 0, 1, 2, \ldots$, in the first half-step of the ADI process, by taking step size $\Delta t/2$. At time level l (the explicit scheme) and $l + 1/2$ (the implicit scheme), the derivatives of ω are discretized in the ξ-direction and η-direction, respectively. i.e.,

$$St\left(\frac{\omega_{i,j}^{l+\frac{1}{2}} - \omega_{i,j}^l}{\Delta t/2}\right) + u_{i,j}\left(\frac{\omega_{i+1,j}^l - \omega_{i-1,j}^l}{2d\xi} - Q_{i,j}\frac{\omega_{i,j+1}^{l+\frac{1}{2}} - \omega_{i,j-1}^{l+\frac{1}{2}}}{2d\eta}\right)$$

$$+ v_{i,j}D_i\frac{\omega_{i,j+1}^{l+\frac{1}{2}} - \omega_{i,j-1}^{l+\frac{1}{2}}}{2d\eta}$$

$$= \frac{g}{Re}\left(\frac{\omega_{i+1,j}^l - \omega_{i,j}^l + \omega_{i-1,j}^l}{(d\xi)^2} - (P_{i,j} - 2Q_{i,j}R_i)\frac{\omega_{i,j+1}^{l+\frac{1}{2}} - \omega_{i,j-1}^{l+\frac{1}{2}}}{2d\eta}\right.$$

$$\left. - 2Q_{i,j}\frac{\omega_{i+1,j+1}^l - \omega_{i+1,j-1}^l - \omega_{i-1,j+1}^l + \omega_{i-1,j-1}^l}{4d\eta d\xi}\right)$$

$$+ \frac{M^2}{Re}D_i^2\frac{\psi_{i,j+1} - 2\psi_{i,j} + \psi_{i,j-1}}{(d\eta)^2} + ReD_a^2\omega_{i,j}^{l+\frac{1}{2}}. \quad (39)$$

After rearranging, Eq. (39) takes the form

$$A(j)\omega_{i,j-1}^{l+\frac{1}{2}} + B(j)\omega_{i,j}^{l+\frac{1}{2}} + C(j)\omega_{i,j+1}^{l+\frac{1}{2}} = S(j), \quad (40)$$

where

$$A(j) = u_{i,j}\frac{Q_{i,j}}{2d\eta} - v_{i,j}\frac{D_i}{2d\eta} - g\frac{P_{i,j} - 2Q_{i,j}R_i}{2d\eta Re} - g\frac{Q_{i,j}^2 + D_i^2}{Re(d\eta)^2}$$

$$B(j) = \frac{St}{\Delta t/2} + g\frac{2\left(Q_{i,j}^2 + D_i^2\right)}{Re(d\eta)^2} - ReD_a^2,$$

$$C(j) = -u_{i,j}\frac{Q_{i,j}}{2d\eta} + v_{i,j}\frac{D_i}{2d\eta} + g\frac{P_{i,j} - 2Q_{i,j}R_i}{2d\eta Re} - g\frac{Q_{i,j}^2 + D_i^2}{Re(d\eta)^2},$$

$$S(j) = \left(\frac{u_{i,j}}{2d\xi} + \frac{g}{Re(d\xi)^2}\right)\omega_{i-1,j} + \left(-\frac{u_{i,j}}{2d\xi} + \frac{g}{Re(d\xi)^2}\right)\omega_{i+1,j}$$

$$+ \frac{St}{\Delta t/2}\omega_{i,j} - \frac{2g}{Re(d\xi)^2}\omega_{i,j}$$

$$- \frac{2g}{Re}Q_{i,j}\frac{\omega_{i+1,j+1}^l - \omega_{i+1,j-1}^l - \omega_{i-1,j+1}^l + \omega_{i-1,j-1}^l}{4d\eta d\xi}$$

$$+ \frac{M^2}{Re}D_i^2\frac{\psi_{i,j+1} - 2\psi_{i,j} + \psi_{i,j-1}}{(d\eta)^2}, \quad (41)$$

For every $i = 2, 3, \ldots, n-1$, Eq. (40) represents a linear tridiagonal system (for $j = 2, 3, \ldots, m-1$). TDMA with the over-relaxation parameter $\lambda = 1.3$ is used for solving the system.

The solution is computed at the time level $l + 1$ using the solution at the time level $l + 1/2$, for $l = 0, 1, 2, \ldots$, in the second half-step of the ADI process, by taking step size $\Delta t/2$. At time level $l + 1/2$ (the explicit scheme) and $l + 1$ (the implicit scheme), the derivatives of ω are discretized in the η-direction and ξ-direction, respectively, i.e.,

$$St\left(\frac{\omega_{i,j}^{l+1} - \omega_{i,j}^{l+\frac{1}{2}}}{\Delta t/2}\right) + u_{i,j}\left(\frac{\omega_{i+1,j}^{l+1} - \omega_{i-1,j}^{l+1}}{2d\xi} - Q_{i,j}\frac{\omega_{i,j+1}^{l+\frac{1}{2}} - \omega_{i,j-1}^{l+\frac{1}{2}}}{2d\eta}\right)$$

$$+ v_{i,j}D_i\frac{\omega_{i,j+1}^{l+\frac{1}{2}} - \omega_{i,j-1}^{l+\frac{1}{2}}}{2d\eta}$$

$$= \frac{g}{Re}\left(\frac{\omega_{i+1,j}^{l+1} - \omega_{i,j}^{l+1} + \omega_{i-1,j}^{l+1}}{(d\xi)^2} - (P_{i,j} - 2Q_{i,j}R_i)\frac{\omega_{i,j+1}^{l+\frac{1}{2}} - \omega_{i,j-1}^{l+\frac{1}{2}}}{2d\eta}\right.$$

$$\left. - 2Q_{i,j}\frac{\omega_{i+1,j+1}^{l+\frac{1}{2}} - \omega_{i+1,j-1}^{l+\frac{1}{2}} - \omega_{i-1,j+1}^{l+\frac{1}{2}} + \omega_{i-1,j-1}^{l+\frac{1}{2}}}{4d\eta d\xi}\right)$$

$$+ \frac{M^2}{Re}D_i^2\frac{\psi_{i,j+1} - 2\psi_{i,j} + \psi_{i,j-1}}{(d\eta)^2} + ReD_a^2\omega_{i,j}^{l+1}. \quad (42)$$

After rearranging, Eq. (42) takes the form

$$\tilde{A}(i)\omega_{i-1,j}^{l+1} + \tilde{B}(i)\omega_{i,j}^{l+1} + \tilde{C}(i)\omega_{i+1,j}^{l+1} = \tilde{S}(i), \quad (43)$$

where

$$\tilde{A}(i) = \frac{-u_{i,j}}{2d\xi} - \frac{2g}{Re(d\xi)^2},$$

$$\tilde{B}(i) = \frac{St}{\Delta t/2} + \frac{2g}{Re(d\xi)^2} - ReD_a^2,$$

$$\tilde{C}(i) = \frac{u_{i,j}}{2d\xi} - \frac{g}{Re(d\xi)^2},$$

$$\tilde{S}(i) = \left(\frac{v_{i,j}D_i}{2d\eta} + g\frac{P_{i,j} - 2Q_{i,j}R_i}{2d\eta Re} + g\frac{Q_{i,j}^2 + D_i^2}{(d\eta)^2} - \frac{u_{i,j}Q_{i,j}}{2d\eta} \right)\omega_{i,j-1}^{l+\frac{1}{2}}$$

$$+ \left(-\frac{v_{i,j}D_i}{2d\eta} - g\frac{P_{i,j} - 2Q_{i,j}R_i}{2d\eta Re} + g\frac{Q_{i,j}^2 + D_i^2}{Re(d\eta)^2} + \frac{u_{i,j}Q_{i,j}}{2d\eta} \right)\omega_{i-1,j+1}^{l+\frac{1}{2}}$$

$$+ \frac{St}{\Delta t/2}\omega_{i,j}^{l+\frac{1}{2}} - 2g\frac{Q_{i,j}^2 + D_i^2}{Re(d\eta)^2}$$

$$- \frac{2g}{Re}Q_{i,j}\frac{\omega_{i+1,j+1}^{l+\frac{1}{2}} - \omega_{i+1,j-1}^{l+\frac{1}{2}} - \omega_{i-1,j+1}^{l+\frac{1}{2}} + \omega_{i-1,j-1}^{l+\frac{1}{2}}}{4d\eta d\xi}$$

$$+ \frac{M^2}{Re}D_i^2\frac{\psi_{i,j+1} - 2\psi_{i,j} + \psi_{i,j-1}}{(d\eta)^2}. \quad (44)$$

For every $j = 2, 3, \ldots, n - 1$, Eq. (43) represents a linear tridiagonal system (for $i = 2, 3, \ldots, m - 1$). TDMA with the over-relaxation parameter $\lambda = 1.3$ is used for solving the system.

For solving Eq. (22), the solution is achieved at the time level $(l + 1/2)$ using the solution at the time level l, for $l = 0, 1, 2, \ldots$, in the first half-step of the ADI process, by taking step size $\Delta t/2$. At time level l (the explicit scheme) and $l + 1/2$ (the implicit scheme), the derivatives of ω are discretized in the ξ-direction and η-direction, respectively, i.e.,

$$St\left(\frac{\theta_{i,j}^{l+\frac{1}{2}} - \theta_{i,j}^l}{\Delta t/2} \right) + u_{i,j}\left(\frac{\theta_{i+1,j}^l - \theta_{i-1,j}^l}{2d\xi} - Q_{i,j}\frac{\theta_{i,j+1}^{l+\frac{1}{2}} - \theta_{i,j-1}^{l+\frac{1}{2}}}{2d\eta} \right)$$

$$+ v_{i,j}D_i\frac{\theta_{i,j+1}^{l+\frac{1}{2}} - \theta_{i,j-1}^{l+\frac{1}{2}}}{2d\eta}$$

$$= \frac{1}{RePr}\left(\frac{\theta_{i+1,j}^l - 2\theta_{i,j}^l + \theta_{i-1,j}^l}{(d\xi)^2} - (P_{i,j} - 2Q_{i,j}R_i) \right.$$

$$\times \frac{\theta_{i,j+1}^{l+\frac{1}{2}} - \theta_{i,j-1}^{l+\frac{1}{2}}}{2d\eta}$$

$$- 2Q_{i,j}\frac{\theta_{i+1,j+1}^l - \theta_{i+1,j-1}^l - \theta_{i-1,j+1}^l + \theta_{i-1,j-1}^l}{4d\eta d\xi}$$

$$\left. + (Q_i^2 + D_i^2 + RdD_i^2)\frac{\theta_{i,j+1}^{l+\frac{1}{2}} - 2\theta_{i,j}^{l+\frac{1}{2}} + \theta_{i,j-1}^{l+\frac{1}{2}}}{(d\eta)^2} \right). \quad (45)$$

After rearranging, Eq. (45) takes the form

$$\overline{A}(j)\theta_{i,j-1}^{l+\frac{1}{2}} + \overline{B}(j)\theta_{i,j}^{l+\frac{1}{2}} + \overline{C}(j)\theta_{i,j+1}^{l+\frac{1}{2}} = \overline{S}(j), \quad (46)$$

where

$$\overline{A}(j) = u_{i,j}\frac{Q_{i,j}}{2d\eta} - v_{i,j}\frac{D_i}{2d\eta} - \frac{P_{i,j} - 2Q_{i,j}R_i}{2d\eta RePr} - \frac{Q_{i,j}^2 + D_i^2 + RdD_i^2}{RePr(d\eta)^2},$$

$$\overline{B}(j) = \frac{St}{\Delta t/2} + \frac{2(Q_{i,j}^2 + D_i^2 + RdD_i^2)}{RePr(d\eta)^2},$$

$$\overline{C}(j) = -u_{i,j}\frac{Q_{i,j}}{2d\eta} + v_{i,j}\frac{D_i}{2d\eta} + \frac{P_{i,j} - 2Q_{i,j}R_i}{2d\eta RePr} - \frac{Q_{i,j}^2 + D_i^2 + RdD_i^2}{RePr(d\eta)^2},$$

$$\overline{S}(j) = \left(\frac{u_{i,j}}{2d\xi} + \frac{1}{RePr(d\xi)^2} \right)\theta_{i-1,j} + \left(-\frac{u_{i,j}}{2d\xi} + \frac{1}{RePr(d\xi)^2} \right)\theta_{i+1,j}$$

$$+ \frac{St}{\Delta t/2}\theta_{i,j} - \frac{1}{RePr(d\xi)^2}\theta_{i,j}$$

$$- \frac{2}{RePr}Q_{i,j}\frac{\theta_{i+1,j+1}^l - \theta_{i+1,j-1}^l - \theta_{i-1,j+1}^l + \theta_{i-1,j-1}^l}{4d\eta d\xi}. \quad (47)$$

For every $i = 2, 3, \ldots, n - 1$, Eq. (46) represents a linear tridiagonal system (for $j = 2, 3, \ldots, m - 1$). TDMA with the over-relaxation parameter $\lambda = 1.3$ is used for solving the system.

The solution is computed at the time level $l + 1$ using the solution at the time level $l + 1/2$, for $l = 0, 1, 2, \ldots$, in the second half-step of the ADI process, by taking step size $\Delta t/2$. At time level $l + 1/2$ (the explicit scheme) and $l + 1$ (the implicit scheme), the derivatives of ω are discretized in the η-direction and ξ-direction, respectively, i.e.,

$$St\left(\frac{\theta_{i,j}^{l+1} - \theta_{i,j}^{l+\frac{1}{2}}}{\Delta t/2} \right) + u_{i,j}\left(\frac{\theta_{i+1,j}^{l+1} - \theta_{i-1,j}^{l+1}}{2d\xi} - Q_{i,j}\frac{\theta_{i,j+1}^{l+\frac{1}{2}} - \theta_{i,j-1}^{l+\frac{1}{2}}}{2d\eta} \right)$$

$$+ v_{i,j}D_i\frac{\theta_{i,j+1}^{l+\frac{1}{2}} - \theta_{i,j-1}^{l+\frac{1}{2}}}{2d\eta}$$

$$= \frac{1}{RePr}\left(\frac{\theta_{i+1,j}^{l+1} - 2\theta_{i,j}^{l+1} + \theta_{i-1,j}^{l+1}}{(d\xi)^2} - (P_{i,j} - 2Q_{i,j}R_i)\frac{\theta_{i,j+1}^{l+\frac{1}{2}} - \theta_{i,j-1}^{l+\frac{1}{2}}}{2d\eta} \right.$$

$$- 2Q_{i,j}\frac{\theta_{i+1,j+1}^{l+\frac{1}{2}} - \theta_{i+1,j-1}^{l+\frac{1}{2}} - \theta_{i-1,j+1}^{l+\frac{1}{2}} + \theta_{i-1,j-1}^{l+\frac{1}{2}}}{4d\eta d\xi}$$

$$\left. + (Q_i^2 + D_i^2 + RdD_i^2)\frac{\theta_{i,j+1}^{l+\frac{1}{2}} - 2\theta_{i,j}^{l+\frac{1}{2}} + \theta_{i,j-1}^{l+\frac{1}{2}}}{(d\eta)^2} \right). \quad (48)$$

After rearranging, Eq. (48) takes the form

$$\overline{\overline{A}}(i)\theta_{i-1,j}^{l+1} + \overline{\overline{B}}(i)\theta_{i,j}^{l+1} + \overline{\overline{C}}(i)\theta_{i+1,j}^{l+1} = \overline{\overline{S}}(i), \quad (49)$$

where

$$\overline{\overline{A}}(i) = \frac{-u_{i,j}}{2d\xi} - \frac{1}{RePr(d\xi)^2},$$

$$\overline{\overline{B}}(i) = \frac{St}{\Delta t/2} + \frac{2}{RePr(d\xi)^2},$$

$$\overline{\overline{C}}(i) = \frac{u_{i,j}}{2d\xi} - \frac{1}{RePr(d\xi)^2},$$

$$\bar{\bar{S}}(i) = \left(\frac{v_{i,j}D_i}{2d\eta} + \frac{P_{i,j} - 2Q_{i,j}R_i}{2d\eta RePr} + \frac{Q_{i,j}^2 + D_i^2 + RdD_i^2}{(d\eta)^2 RePr} - \frac{u_{i,j}Q_{i,j}}{2d\eta} \right) \theta_{i,j-1}^{l+\frac{1}{2}}$$

$$+ \left(-\frac{v_{i,j}D_i}{2d\eta} - \frac{P_{i,j} - 2Q_{i,j}R_i}{2d\eta RePr} + \frac{Q_{i,j}^2 + D_i^2 + RdD_i^2}{RePr(d\eta)^2} + \frac{u_{i,j}Q_{i,j}}{2d\eta} \right) \theta_{i,j+1}^{l+\frac{1}{2}}$$

$$+ \frac{St}{\Delta t/2}\theta_{i,j}^{l+\frac{1}{2}} - 2\frac{Q_{i,j}^2 + D^2{}_i + RdD_i^2}{RePr(d\eta)^2}\theta_{i,j}^{l+\frac{1}{2}}$$

$$- \frac{2}{RePr}Q_{i,j}\frac{\theta_{i+1,j+1}^{l+\frac{1}{2}} - \theta_{i+1,j-1}^{l+\frac{1}{2}} - \theta_{i-1,j+1}^{l+\frac{1}{2}} + \theta_{i-1,j-1}^{l+\frac{1}{2}}}{4d\eta d\xi}. \quad (50)$$

For every $j = 2, 3, \ldots, n - 1$, Eq. (49) represents a linear tridiagonal system (for $i = 2, 3, \ldots, m - 1$). TDMA with the over-relaxation parameter $\lambda = 1.3$ is used for solving the system.

IV. RESULTS AND DISCUSSION

The stream-wise axial velocity (u) and temperature (θ) profiles are obtained for M, St, β, Da, Pr, and Rd by solving Eqs. (20)–(22), subject to the conditions, as mentioned in Sec. II. The computations for the present article are carried out in serial on an ordinary personal computer. The computations can be accelerated through
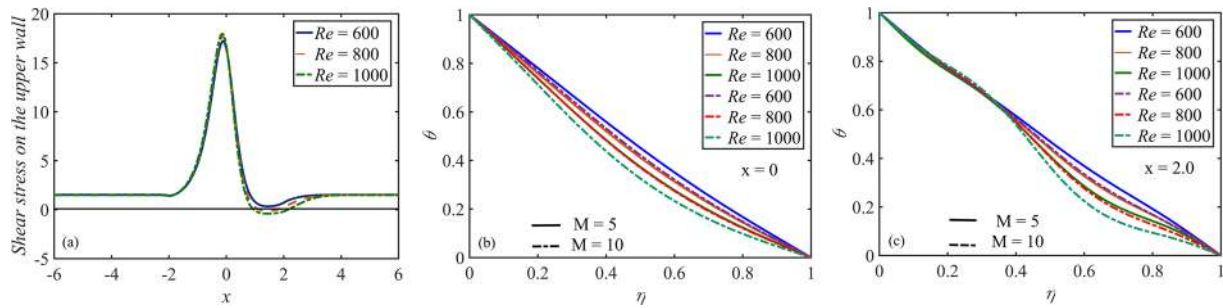

FIG. 2. Flow profiles for different values of Reynolds number Re at t = 0.25 with M = 5, β = 0.5, D_a = 0.002, Pr = 1, and Rd = 1: (a) the WSS distribution, (b) temperature profile θ vs η at x = 0, and (c) temperature profile θ vs η at x = 2.
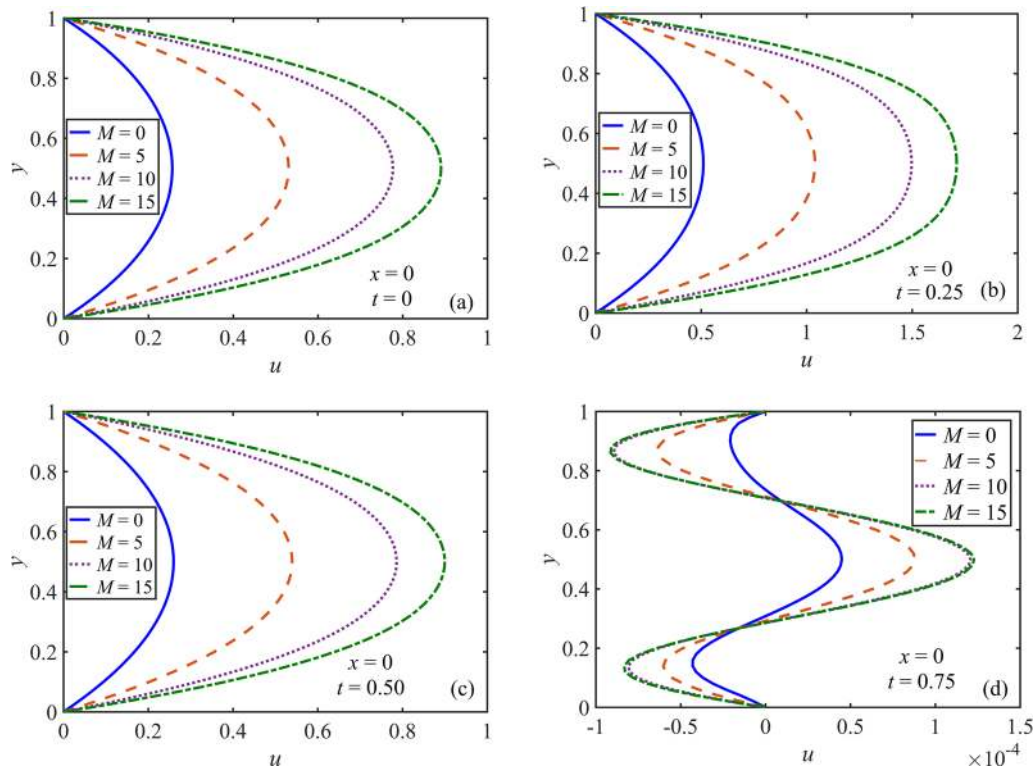

FIG. 3. Velocity profile u vs y for different values of the Hartman number M at x = 0 with St = 0.02, β = 0.5, D_a = 0.002, Pr = 1, and Rd = 1: (a) at t = 0, (b) at t = 0.25, (c) at t = 0.5, and (d) at t = 0.75.
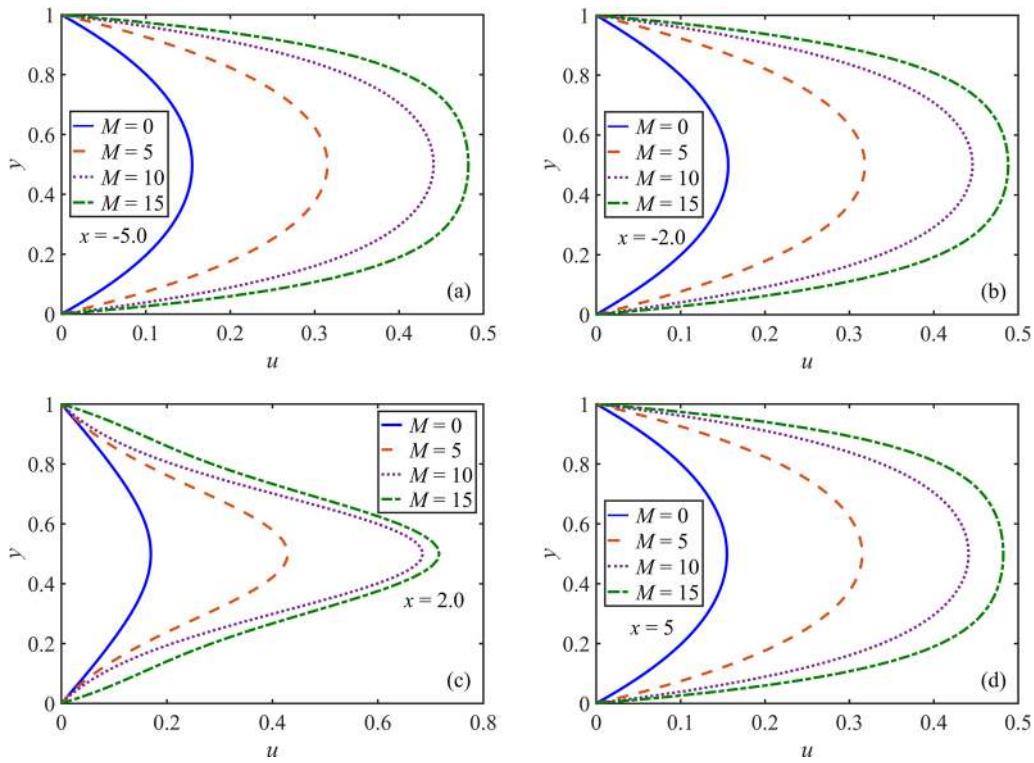
FIG. 4. Velocity profile u vs y for different values of the Hartman number M at time t = 0.25 with St = 0.02, β = 0.5, D_a = 0.002, Pr = 1, and Rd = 1: (a) at x = −5, (b) at x = −2, (c) at x = 2, and (d) at x = 5.
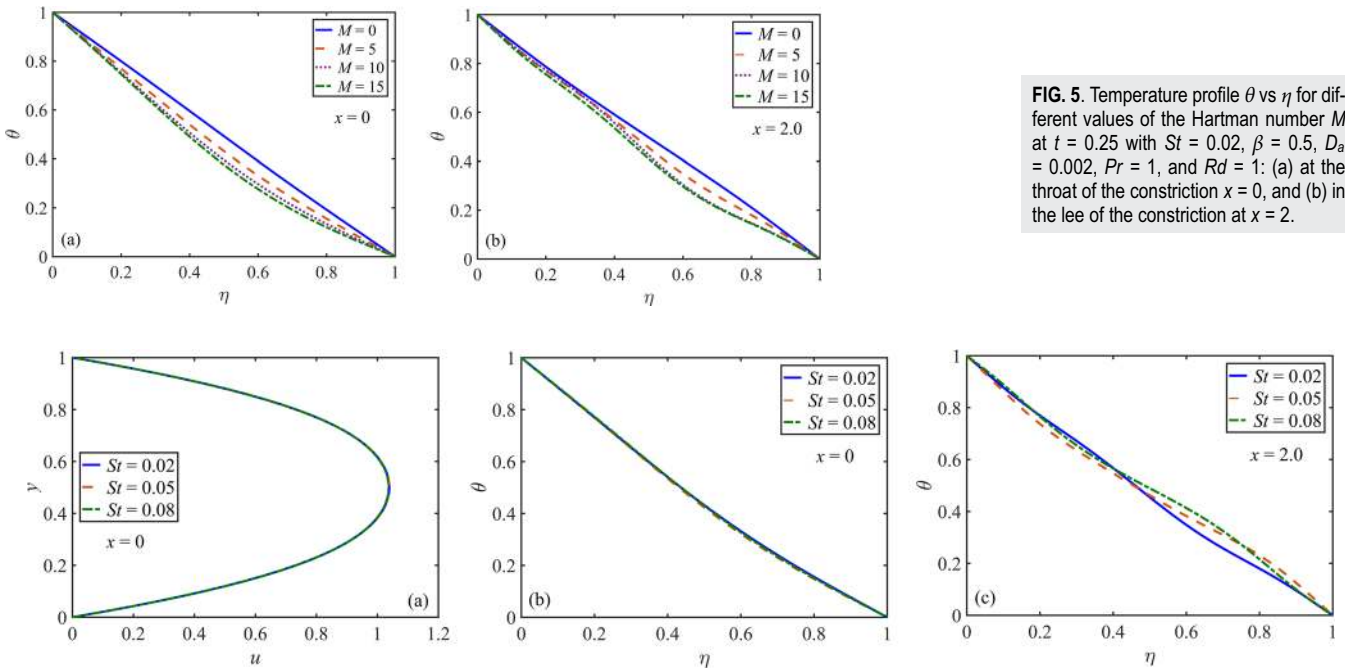

FIG. 5. Temperature profile θ vs η for different values of the Hartman number M at t = 0.25 with St = 0.02, β = 0.5, D_a = 0.002, Pr = 1, and Rd = 1: (a) at the throat of the constriction x = 0, and (b) in the lee of the constriction at x = 2.

FIG. 6. Flow profiles for different values of the Strouhal number St at t = 0.25 with M = 5, β = 0.5, D_a = 0.002, Pr = 1, and Rd = 1: (a) velocity profile u vs y at x = 0, (b) temperature profile θ vs η at x = 0, (c) temperature profile θ vs η at x = 2.

parallel programming of the method and, then, executing on a high-performance parallel architecture.[42] Unless stated otherwise, Reynolds number (Re) is set as 700 for the computations. The impact of the flow parameters is studied for four different time levels, i.e., the start of the pulsating motion ($t = 0.0$), the maximum flow rate ($t = 0.25$), the minimum flow rate ($t = 0.50$), and the instantaneous zero net flow ($t = 0.75$).

The WSS is computed for Re = 600, 800, 1000 with $M = 5$, $St = 0.02$, $\beta = 0.5$, $D_a = 0.002$, $Pr = 1$, and $Rd = 1$. The WSS is maximum at $x = 0$ (where the flow rate is maximum) and is symmetric at the upper and lower walls. The WSS at the upper wall for $t = 0.25$ is shown in Fig. 2(a). Higher values of Re result in higher WSS at $x = 0$, i.e., the throat of the constriction. There is a flow separation

region in the wake of the constriction that expands on increasing Re. Consequently, the WSS decreases there at the walls. The θ profiles for distinct values of Re at $x = 0$ and $x = 2$ are shown in Figs. 2(b) and 2(c), respectively, for $t = 0.25$. For higher values of Re and M, the temperature decreases at $x = 0$. However, at $x = 2$, no significant reduction in the temperature is noted in the lower half of the channel.

The u and θ profiles, computed for $M = 0, 5, 10, 15$ with $St = 0.02$, $\beta = 0.5$, $D_a = 0.002$, $Pr = 1$, and $Rd = 1$, are shown in Figs. 3–5. The u profile at $x = 0$ is shown in Fig. 3 for the four time instants. The velocity attains its maximum value at $x = 0$. The peak value of u increases with M, and the curves exhibit a parabolic profile at $0 \leq t \leq 0.5$. However, at $t = 0.75$,
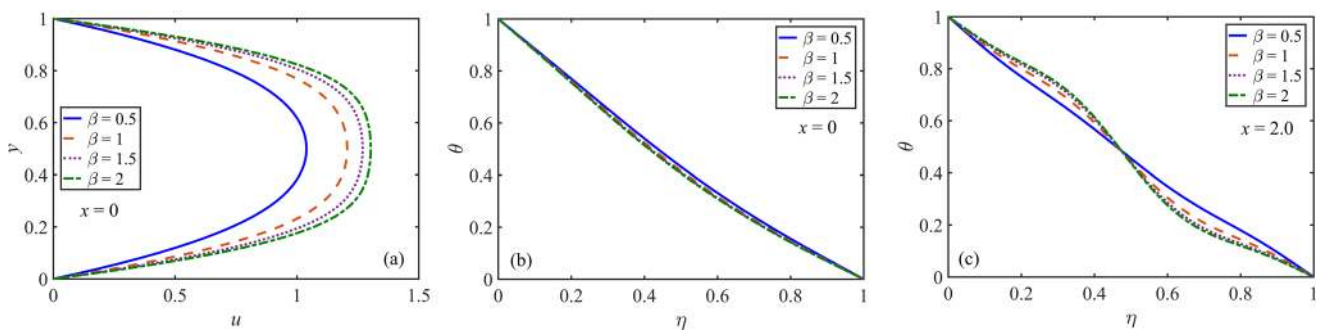

FIG. 7. Flow profiles for different values of the CF parameter β at $t = 0.25$ with $M = 5$, $St = 0.02$, $D_a = 0.002$, $Pr = 1$, and $Rd = 1$: (a) velocity profile u vs y at $x = 0$, (b) temperature profile θ vs η at $x = 0$, and (c) temperature profile θ vs η at $x = 2$.
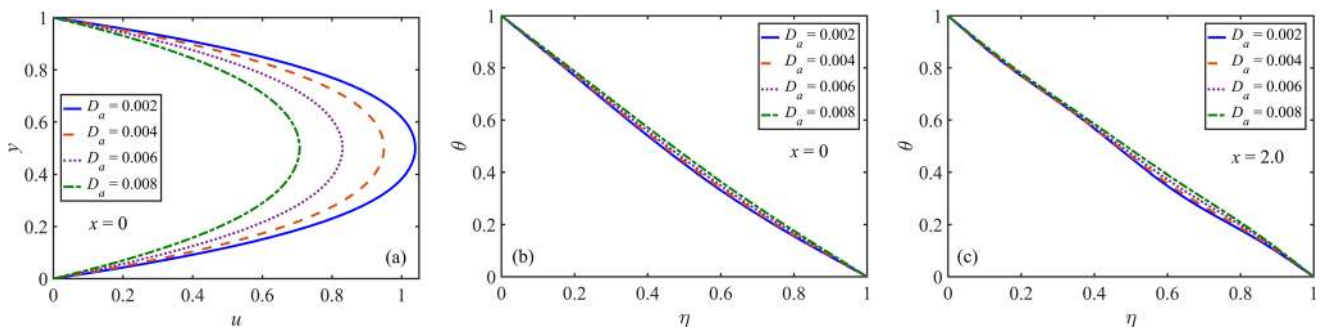

FIG. 8. Flow profiles for different values of the porosity parameter D_a at $t = 0.25$ with $M = 5$, $St = 0.02$, $\beta = 0.5$, $Pr = 1$, and $Rd = 1$: (a) velocity profile u vs y at $x = 0$, (b) temperature profile θ vs η at $x = 0$, and (c) temperature profile θ vs η at $x = 2$.
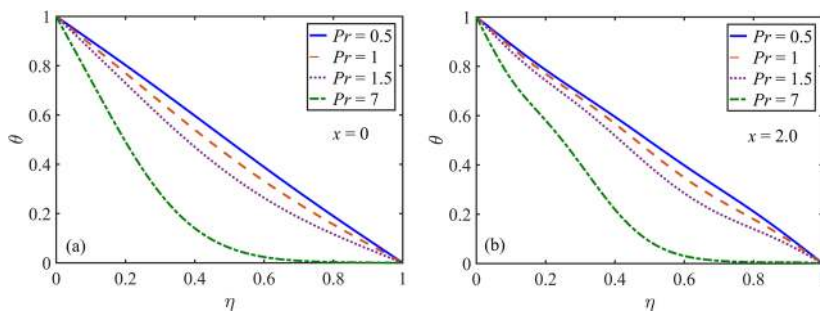

FIG. 9. Temperature profile θ vs η for different values of the Prandtl number Pr at $t = 0.25$ with $M = 5$, $St = 0.02$, $\beta = 0.5$, $D_a = 0.002$, and $Rd = 1$: (a) at the throat of the constriction $x = 0$ and (b) in the lee of the constriction at $x = 2$.
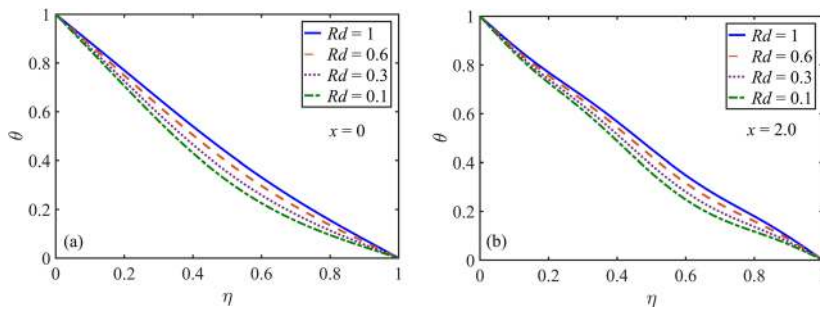
FIG. 10. Temperature profile θ vs η for different values of the thermal radiation parameter Rd at $t = 0.25$ with $M = 5$, $St = 0.02$, $\beta = 0.5$, $D_a = 0.002$, and $Pr = 1$: (a) at the throat of the constriction $x = 0$, and (b) in the lee of the constriction at $x = 2$.

the magnitude of u is substantially less as compared to all the other time instants. Moreover, a backflow is observed in the vicinity of the walls. Next, the velocity profiles at four different x-locations for $t = 0.25$ are shown in Fig. 4. The profiles are parabolic at all locations except at $x = 2.0$, where the constriction ends downstream of the center.

The θ profiles against M at the throat of the constriction, i.e., $x = 0$, and in the lee of the constriction, specifically $x = 2$, are shown in Fig. 5 for $t = 0.25$. The value of θ decreases as M is increased. Further analysis revealed that the minimum and maximum values of θ are at $t = 0.50$ and $t = 0.75$, respectively, for $M > 0$. Upstream of the constriction, the temperature decreases with an increase in M. However, although somewhat similar, this behavior is not perfectly uniform downstream of the constriction. This is due to the separation of flow and the generation of the vortices downstream of the constriction.
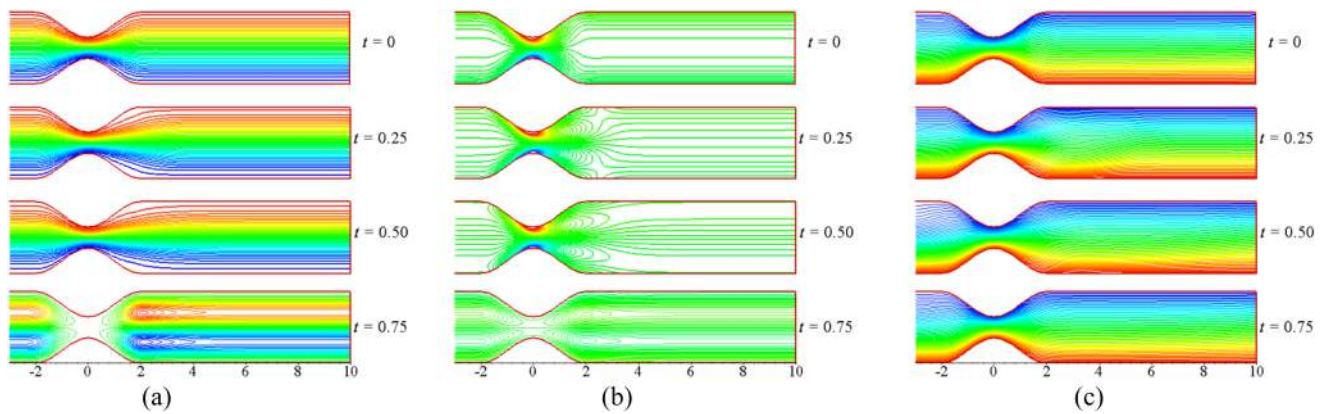

FIG. 11. (a) Streamlines, (b) vorticity, and (c) temperature distribution plots at different instants of a pulse cycle with Re = 800, $M = 5$, $St = 0.02$, $\beta = 0.5$, $D_a = 0.002$, $Pr = 1$, and $Rd = 1$.
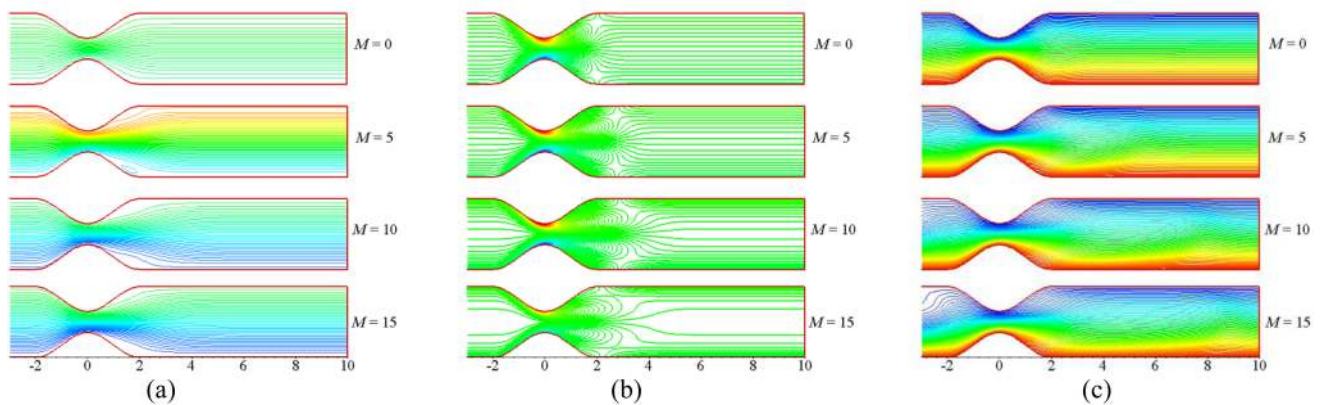

FIG. 12. (a) Streamlines, (b) vorticity, and (c) temperature distribution plots for different values of the Hartman number M at $t = 0.25$ with Re = 1000, $St = 0.02$, $\beta = 0.5$, $D_a = 0.002$, $Pr = 1$, and $Rd = 1$.

The u and θ profiles are computed for St = 0.02, 0.05, 0.08 with M = 5, β = 0.5, D_a = 0.002, Pr = 1, and Rd = 1. Figure 6(a) shows the u profile at x = 0 and t = 0.25, where u attains its maximum value due to the maximum flow rate. For $0 \le t \le 0.5$, no significant variation in u is observed on varying St at x = 0; however, the peak value of u decreases on increasing St at the other x locations. The profiles are parabolic at most of the x-locations except at x = 2. The θ profiles against St at x = 0 and x = 2 are shown in Figs. 6(b) and 6(c), respectively, for t = 0.25. There are no significant variations in the profiles at x = 0; however, slight fluctuations in the profile are noted at x = 2.

The u and θ profiles are computed for β = 0.5, 1, 1.5, 2 with M = 5, St = 0.02, D_a = 0.002, Pr = 1, and Rd = 1. Figure 7(a) shows u profiles at x = 0 and t = 0.25. The u profiles against β are somewhat similar to the case of increasing M, except for the profile at x = 2 for which there is some backflow near the walls on increasing β. The θ

profiles against β at x = 0 and x = 2 are shown in Figs. 7(b) and 7(c), respectively, for t = 0.25. Again the θ profiles are somewhat similar to the case of increasing M, except for the θ profile at x = 2 [Fig. 7(c)] for which there is a reversal of behavior against β in the upper and lower half of the channel.

The u and θ profiles, computed for D_a = 0.002, 0.004, 0.006, 0.008 with M = 5, St = 0.02, β = 0.5, Pr = 1, and Rd = 1, are shown in Fig. 8, for t = 0.25. The trends of the profiles on increasing D_a are very much similar to the cases of decreasing M.

The θ profile, computed for Pr = 0.5, 1.0, 1.5, 7.0 with M = 5, St = 0.02, β = 0.5, D_a = 0.002, and Rd = 1, is shown in Fig. 9, for t = 0.25. The temperature decreases with increasing values of Pr. However, slight fluctuations in the temperature profiles are observed downstream of the constriction.

The θ profile, computed for Rd = 1, 0.6, 0.3, 0.1 with M = 5, St = 0.02, β = 0.5, and Pr = 1, is shown in Fig. 10, for t = 0.25. The
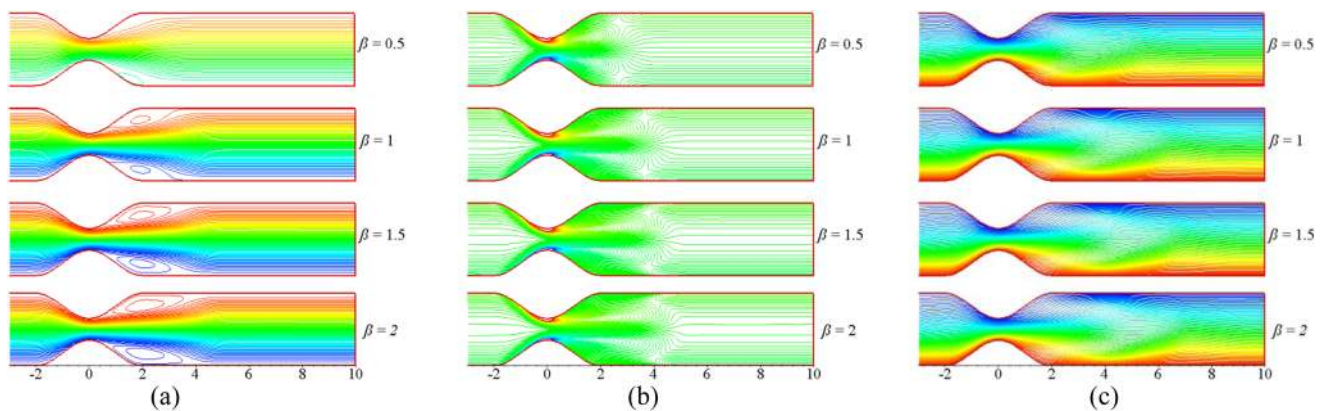

FIG. 13. (a) Streamlines, (b) vorticity, and (c) temperature distribution plots for different values of the CF parameter β at t = 0.25 with Re = 1000, M = 5, St = 0.02, D_a = 0.002, Pr = 1, and Rd = 1.
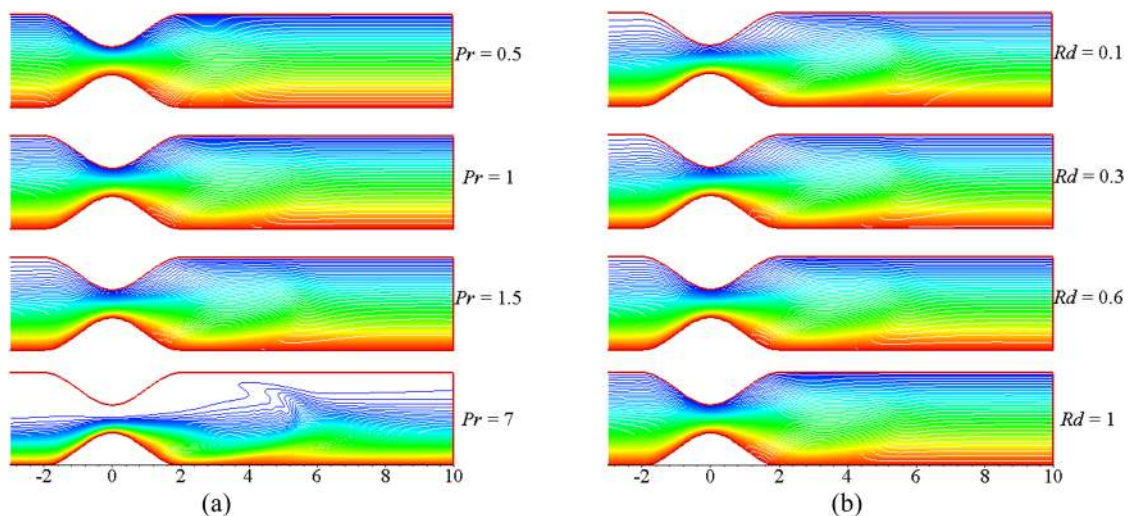

FIG. 14. The temperature distribution plots at t = 0.25 with Re = 1000, M = 5, St = 0.02, β = 0.5, and D_a = 0.002: (a) for different values of Prandtl number Pr and Rd = 1, and (b) for different values of Prandtl number Rd and Pr = 1.

temperature increases with increasing values of Rd. However, the profiles slightly fluctuate downstream of the constriction.

To further elaborate the flow profiles, the plots of the streamlines, vorticity, and temperature distribution at the four time levels $t = 0, 0.25, 0.5, 0.75$ are shown in Fig. 11. The plots of the streamlines, vorticity, and temperature distribution at $t = 0.25$ for different values of M and β are shown in Figs. 12 and 13, respectively. The temperature distribution plots for different values of Pr and Rd, at $t = 0.25$, are shown in Figs. 14(a) and 14(b), respectively.

V. CONCLUDING REMARKS

The pulsatile flow of thermally developed non-Newtonian CF in a channel with constricted walls under the impact of the magnetic field is numerically investigated. The effects of the magnetic field parameter or Hartman number (M), pulsatile flow parameter or Strouhal number (St), CF parameter (β), Darcy parameter or porosity parameter (D_a), Prandtl number (Pr), and thermal radiation parameter (Rd) on the axial velocity (u) and dimensionless temperature (θ) profiles are observed. The summary of the findings is as follows:

- The wall shear stress (WSS) is maximum at the throat of the constriction (where the flow rate is maximum), and it increases with an increase in Re. The WSS is symmetrical at the upper and lower walls.
- On increasing M, the stream-wise axial velocity increases. At all places, the profiles are parabolic except at $x = 2$. On increasing M, the temperature decreases at the throat of the constriction and upstream of the constriction. However, this behavior is not perfectly uniform downstream of the constriction.
- On increasing St, no significant variation in u is observed at $x = 0$. However, the peak value of the velocity decreases slightly at the other x locations of the channel for $0 \leq t \leq 0.5$. At all places, the profiles are parabolic except at $x = 2$. On increasing St, there are no significant variations in the temperature profiles at $x = 0$; however, slight fluctuations in the profile are noted at $x = 2$.
- On increasing β, the velocity and temperature profiles, for most of the cases considered, exhibit a behavior similar to that for increasing M. Slight fluctuations in the profiles are observed downstream of the constriction.
- On increasing D_a, the velocity and temperature profiles, for most of the cases considered, exhibit a behavior similar to that for decreasing M.
- On increasing Pr, the temperature decreases. That is, the flow has a thinner thermal boundary layer with a larger Prandtl number. However, slight fluctuations in the temperature profiles are observed downstream of the constriction.
- On increasing Rd, the temperature increases. However, slight fluctuations in the temperature profiles are observed downstream of the constriction.

For understanding of blood flow in stenotic arteries, designing biomechanical structures, and use in industrial facilities where flow pulsation plays a vital role, these results can be beneficial for scientists and engineers.

DATA AVAILABILITY

The data that support the findings of this study are available within the article.

REFERENCES

[1] T. S. Lee, J. Fluids Eng. **116**, 66–71 (1994).
[2] H. Huwang and B. R. Seymour, Comput. Fluids **24**, 153–160 (1995).
[3] T. R. Mahapatra, G. C. Layek, and M. K. Maiti, Int. J. Nonlinear Mech. **37**, 171–186 (2002).
[4] O. R. Tutty, J. Biomech. Eng. **114**, 50–54 (1992).
[5] R. Mittal, S. P. Simmons, and F. Najjar, J. Fluid Mech. **485**, 337–378 (2003).
[6] J. Isler, R. Gioria, and B. Carmo, J. Fluid Mech. **866**, R4 (2019).
[7] S. Bandyopadhyay and G. C. Layek, Commun. Nonlinear Sci. Numer. Simul. **17**, 2434–2446 (2012).
[8] C. Clark, J. Biomech. **9**, 521–528 (1976).
[9] A. Shirai and S. Masuda, PloS One **8**, e59416 (2013).
[10] S. Chakravarty, P. K. Mandal, and Sarifuddin, Int. J. Nonlinear Mech. **40**, 1268–1281 (2005).
[11] H. Liu and T. Yamaguchi, J. Biomech. Eng. **123**, 88–96 (2001).
[12] A. Khair, B.-C. Wang, and D. C. S. Kuhn, Int. J. Comput. Fluid Dyn. **29**, 447–463 (2015).
[13] A. V. Hirtum, Mech. Res. Commun. **83**, 53–57 (2017).
[14] N. Mustapha, P. K. Mandal, P. R. Johnston, and N. Amin, Appl. Math. Modell. **34**, 1559–1573 (2010).
[15] N. Casson, *Rheology of Disperse System* (Pergamon Press, Oxford, 1959).
[16] D. S. Sankar and U. Lee, J. Mech. Sci. Technol. **25**, 2573–2581 (2011).
[17] D. S. Sankar, A. K. Nagar, K. K. Viswanathan, and A. V. Kumar, in *7th Brunei International Conference on Engineering and Technology* (BICET, 2018).
[18] R. Bali and U. Awasthi, J. Appl. Math. **03**, 436–441 (2012).
[19] R. Padma, R. T. Selvi, and R. Ponalagusamy, Eur. Phys. J. Plus **134**, 221 (2019).
[20] Z. Iqbal, R. Mehmood, E. Azhar, and Z. Mehmood, Eur. Phys. J. Plus **132**, 175 (2017).
[21] G. J. Reddy, B. Kethireddy, M. Kumar, and M. M. Hoque, J. Mol. Liq. **252**, 245–262 (2018).
[22] G. C. Shit and S. Majee, J. Magn. Magn. Mater. **388**, 106–115 (2015).
[23] M. Massoudi and T. X. Phuoc, Comput. Math. Appl. **56**, 199–211 (2008).
[24] D. S. Sankar and U. Lee, Commun. Nonlinear Sci. **14**, 2971–2981 (2009).
[25] H. Amlimohamadi, M. Akram, and K. Sadeghy, Korea-Aust. Rheol. J. **28**, 129–137 (2016).
[26] C. Tu and M. Deville, J. Biomech. **29**, 899–908 (1996).
[27] T. Moschandreou and M. Zamir, Int. J. Heat. Mass. Transfer **40**, 2461–2466 (1997).
[28] T. H. Ji, S. Y. Kim, and J. M. Hyun, Int. J. Heat Mass Transfer **51**, 1130–1138 (2008).
[29] E. A. M. Elshafei, M. S. Mohamed, H. Mansour, and M. Sakr, Int. J. Heat Fluid Flow **29**, 1029–1038 (2008).
[30] R. Blythman, T. Persoons, N. Jeffers, and D. B. Murray, Int. J. Heat Mass Transfer **128**, 279–289 (2019).

[31] S. Aman, I. I. Khan, Z. Ismail, M. Z. Salleh, A. S. Alshomrani, and M. S. Alghamdi, AIP Adv. **7**, 015036 (2017).

[32] A. Hussanan, M. Z. Salleh, I. Khan, and R. M. Tahar, Teknologi **78**, 8264 (2016).

[33] S. Srinivas, C. K. Kumar, and A. S. Reddy, Nonlinear Anal. Model **23**, 213–233 (2018).

[34] I. Ullah, T. A. Alkanhal, S. Shafie, K. S. Nisar, I. Khan, and O. D. Makinde, Symmetry **11**, 531 (2019).

[35] A. Khan, D. Khan, I. Khan, M. Taj, I. Ullah, A. M. Aldawsari, P. Thounthong, and K. Sooppy Nisar, Symmetry **11**, 1295 (2019).

[36] S. E. Ahmed and A. A. M. Arafa, Phys. Scr. **95**, 095206 (2020).

[37] R. Kumar, R. Kumar, S. A. Shehzad, and A. J. Chamkha, Appl. Math. Mech. **41**, 1651–1670 (2020).

[38] A. Ali, H. Farooq, Z. Abbas, Z. Bukhari, and A. Fatima, Sci. Rep. **10**, 10629 (2020).

[39] I. Pop and M. A. Sheremet, Int. J. Numer. Method Heat Fluid Flow **27**(10), 2318–2332 (2017).

[40] A. Arzani and S. C. Shadden, J. Biomech. **73**, 145–152 (2018).

[41] J. Z. Wu, H. Y. Ma, and M. D. Zhou, in *Vorticity and Vortex Dynamics* (Springer Science+Business Media, 2007).

[42] A. Ali and K. S. Syed, Adv. Comput. **91**, 87–118 (2013).